

C. B. W. Pedersen
e-mail: cbwp2@eng.cam.ac.uk

N. A. Fleck
e-mail: naf@eng.cam.ac.uk

Department of Engineering,
University of Cambridge,
Trumpington Street,
Cambridge, CB2 1PZ,
United Kingdom

G. K. Ananthasuresh
Department of Mechanical Engineering,
Indian Institute of Science,
Bangalore 560012,
India
e-mail: suresh@mecheng.iisc.ernet.in

Design of a Compliant Mechanism to Modify an Actuator Characteristic to Deliver a Constant Output Force

Topology and size optimization methods are used to design compliant mechanisms that produce a constant output force for a given actuator characteristic of linearly decreasing force versus displacement. The design procedure consists of two stages: (i) topology optimization using two-dimensional (2-D) continuum parametrization, and (ii) size optimization of the beam-element abstraction derived from the continuum topology solution. The examples considered are based upon electrostatic microactuators used widely in microsystems. The procedure described here provides conceptual as well as practically usable designs for compliant transmission mechanisms with a constant output force characteristic. For any given topology design, the maximum achievable constant force over a given displacement range is determined. Ideal rigid-body and spring-equipped mechanisms are analyzed and their features are used to compare with the compliant solutions obtained. [DOI: 10.1115/1.2218883]

1 Introduction

Most actuators possess a finite passive stiffness. Consequently, for a given stimulus to the actuator, such as the applied voltage in an electrostatic actuator, the output force decreases with increasing output displacement (i.e., stroke). Huber et al. [1] have summarized the output force versus output displacement characteristics for a wide range of actuators. Most actuators exhibit a variable output force making them unsuitable for applications requiring constant force. Applications requiring constant output force over a range of displacement include devices to handle delicate parts and grips for wear and material testing. Hydraulic and pneumatic actuators can provide a constant force, but have limited suitability, especially in the field of Microelectromechanical Systems (MEMS). Bell et al. [2], in their survey of microactuators, note that the output force typically decreases with increasing stroke. The most widely used microactuator—the electrostatic comb-drive linear actuator—exhibits a linearly, or nonlinearly decreasing force with increasing output displacement for a given applied voltage. A transmission mechanism is needed downstream of the actuator if it is to be used in constant force applications. A compliant mechanism can serve this purpose; it can be fully integrated into the comb drive without complicating the microfabrication process. Related studies on constant force mechanisms are now briefly reviewed.

Constant force mechanisms are not new. For example, Neg'ator springs and other spring-equipped devices are commercially available. Spring-equipped constant force mechanisms also exist (Nathan [3]; Jenuwine and Midha [4]). In recent years, compliant mechanisms, that deliver an almost constant force have been developed (Howell, Midha, and Murphy [5]; Boyle, Howell, Magleby and Evans [6]). These are designed to store energy in such a way that the imposed force is almost constant over a range of displacement. Actively controlled mechanisms are also able to provide constant applied forces of desired magnitude (Nahar and Sugar [7]). The constant force transmission mechanisms presented in this paper differ from all of the above in that a constant output

force is achieved over some stroke by conversion of an actuation force obtained from an actuator of constant stiffness. The level of output force can be made to scale linearly with the stall force of the actuator: the mechanism behaves as a passive but smart open-loop transmission device. Since the proposed transmission mechanism is a compliant mechanism, its constant force characteristic is sufficiently accurate over a prescribed displacement range.

The methodology used to design compliant mechanisms is briefly reviewed as follows. The topology optimization technique has been successfully applied to compliant mechanism design for mechanical and nonmechanical actuation stimuli (Ananthasuresh et al. [7]; Sigmund [8]; Frecker et al. [9]; Bendsøe and Sigmund [10]; Ananthasuresh [11]). In topology optimization, the design of the geometrical form of an elastic structure is posed as a problem of optimal material distribution in a given space. Strategies for topology optimization for finite deflections are discussed by Bruns and Tortorelli [12], Pedersen et al. [13], and Saxena and Ananthasuresh [14], and more recently by Saxena [15], who used genetic algorithms. Pedersen [16–18] also considered the problem of designing optimized structures for prescribed energy absorption and crashworthiness. The methodology adopted in this paper is based upon some of the above studies with suitable enhancements as required. The design variables in most of the published works in this field are concerned with the fictitious density of continuum elements or sizes or cross-section areas of truss and beam elements. Recently, alternate design parametrizations are being explored (e.g., Zhou and Ting [19]; Wang et al. [20]). In this work, continuum element based and frame element based parametrizations are used in two stages to combine the benefits of both.

Problem Statement and Outline of Paper. Figure 1(a) shows typical force versus stroke characteristics $P(u)$ of common actuators. These are taken from the comprehensive survey of Huber et al. [1]. Except for hydraulic and pneumatic actuators, the output force varies with displacement. The internal stiffness of the following actuators is constant: electrostatic, piezoelectric, thermal expansion, and magnetostrictive actuators. Let the stiffness, that is the linear spring constant, of these actuators be denoted by K . And define the stall force P_s of the actuator as the force it produces at zero output displacement. The force P available at the output end

Contributed by the Mechanisms and Robotics Committee of ASME for publication in the JOURNAL OF MECHANICAL DESIGN. Manuscript received June 26, 2005; final manuscript received December 6, 2005. Review conducted by Larry L. Howell.

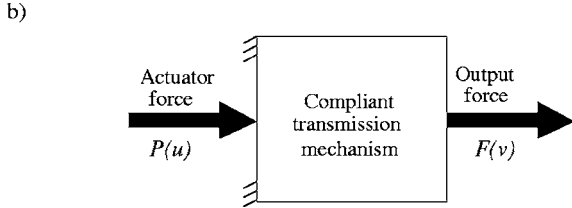
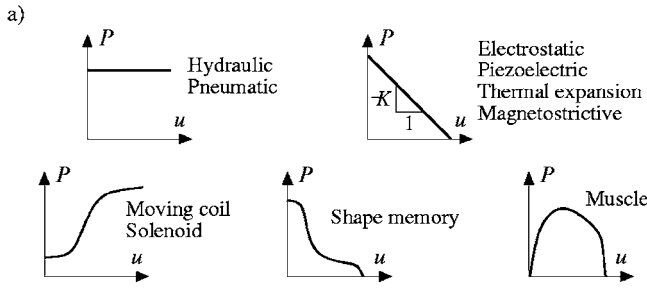


Fig. 1 (a) Examples of actuators and their characteristics. (b) The generation of a desired constant force characteristic by a compliant transmission mechanism.

of the actuator is $P_s - Ku$ in terms of the actuator displacement u . Representative values of the stall force and stiffness of these actuators are listed in Table 1.

Transmission mechanisms are necessary in order to convert a given actuator characteristic into a more desirable characteristic. The transmission mechanisms can be made from either *rigid-body mechanisms* that store no internal energy or from an energy-storing elastic structure, known as *compliant mechanisms* (Howell [21]). Compliant mechanisms can be fabricated over a wide range of length scale, as they do not require assembly from individual components. Although the methodology developed in this paper is applicable to any type of actuator characteristic, as indicated in Fig. 1(b), our focus in the present study is restricted to mechanisms that convert an actuator characteristic of constant stiffness into a characteristic with constant output force.

The paper is organized as follows. In Sec. 2, the design problem for an actuator with constant stiffness is stated. Transmission characteristics are summarized for two baseline, reference cases: an *ideal pin-jointed, rigid-body mechanism* and an *ideal compliant mechanism*. The structural optimization methods used for obtaining designs are described in Sec. 3. It is found that the compliant constant force transmission mechanisms have a highly nonlinear response in order to fulfill the design criteria. Therefore, geometrically nonlinear finite element methods are essential. The preliminary designs of the mechanisms are determined by continuum topology optimization. In Sec. 4, the sensitivity of the *topology optimized designs* to actuator characteristics and the desired output force is examined. It is found that the topology optimized mechanisms contain hinges that resemble torsional springs or frictionless joints (Poulsen [22]; Yin and Ananthasuresh [23]; Rahmatalla and Swan [24]; Bendsoe and Sigmund [10]). Consequently, in Section 5 the topology solutions can be converted into *beam models*, and these are then *size optimized*. In Sec. 6, the size

Table 1 Typical characteristics of MEMS actuators of constants stiffness taken from Bell et al. [2]

| Type of MEMS actuator | Stall force P_s (mN) | Linear stiffness K (N/M) |
|-----------------------|------------------------|----------------------------|
| Comb drive | 0.02 ~ 3 | 2 ~ 400 |
| Thermal | 0.004 ~ 60 | 0.1 ~ 2500 |
| Piezoelectric | 0.01 ~ 2 | 0.1 ~ 100 |
| Magnetostrictive | 0.3 ~ 0.6 | 5 ~ 30 |
| Present work | 0.08 ~ 0.12 | 1 ~ 100 |

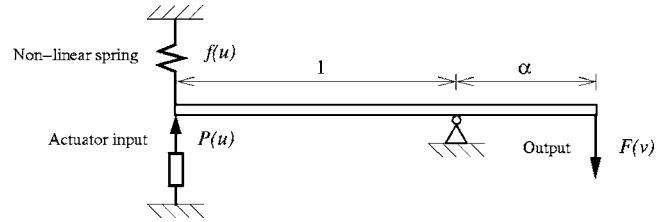


Fig. 2 Spring mechanism with linear kinematics

optimized beam models are validated using continuum finite element modeling by ABAQUS (Hibbitt et al. [25]). Concluding remarks are given in Sec. 6.

2 Ideal Constant Force Mechanisms With no Embodiment

2.1 Pin-Jointed Rigid-Body Mechanism for Constant Stiffness Actuator. It is instructive to benchmark the optimized compliant mechanisms derived later in this study with an ideal rigid-body, pin-jointed mechanism that stores no internal energy. Assume that the input force P from the actuator is related to the input displacement u by $P_s - Ku$, and further assume that the ideal, pin-jointed mechanism is so designed that it can deliver a constant output force F . The dependence of the output displacement v upon u is written as $v = h(u)$. Then, the principle of virtual work for the system in Fig. 1(b) is used to obtain the function $h(u)$:

$$P \delta u = F \delta v \Rightarrow h'(u) = \frac{1}{F} [P_s - Ku] \quad (1)$$

This relation can be integrated immediately, using the boundary condition $h(0) = 0$, to give

$$v = h(u) = \frac{1}{F} \left[P_s u - \frac{1}{2} K u^2 \right]. \quad (2)$$

We conclude that the pin-jointed mechanism can achieve a constant output force F provided it possesses a *quadratic kinematic relation* between the output displacement u and input displacement v . It is clear from (2) that, in principle, a mechanism can be designed to deliver any desired value of constant output force F for any actuator of prescribed P_s and K . This is achieved by tuning the coefficients of the kinematic relation $h(u) = \alpha_1 u + \alpha_2 u^2$ such that $\alpha_1 = P_s / F$ and $\alpha_2 = -K / 2F$. Note that the nonlinear coupling relation $h(u)$ involves the value of stall force P_s . Consequently, any given geometric design of a pin-jointed mechanism can only deliver a constant output force for a single value of stall force. This is a major restriction, apart from the difficulty of designing a suitably non-linear transmission ratio $h(u)$.

2.2 Spring Mechanism With Linear Kinematics. An alternative strategy is to design a linear transmission mechanism with constant gear ratio: the relation between the output displacement v and input displacement u is then of the form $v = \alpha u$, where α is a constant. One strategy to achieve a constant output force F is to introduce a nonlinear spring in parallel with the transmission mechanism, as shown in Fig. 2. Assume that the actuator force $P(u)$ is in equilibrium with the sum of the spring characteristic $f(u)$ and with the transmission force $F(v)$. Then, the principle of virtual work gives

$$P \delta u = f(u) \delta u + F \delta v \Rightarrow F = \frac{P_s - Ku - f(u)}{\alpha}. \quad (3)$$

The output force F is constant when the following relation is fulfilled

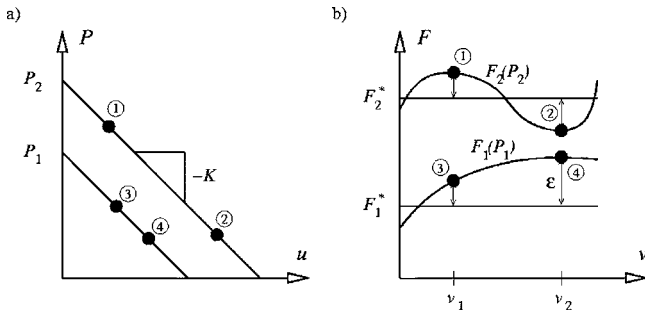


Fig. 3 (a) The characteristic of the actuator of constant stiffness K for two different stall forces P_1 and P_2 . (b) The actual transformed output forces of the compliant mechanism are F_j . In the optimization the errors ϵ between maximized constant forces F_j^* and the actual output forces F_j are minimized in given collocation points of v_j . These collocation points v_j of the collocation points lead through the equilibrium to the corresponding displacements of the actuator indicated by circles on the actuator response.

$$f(u) = c - Ku \Rightarrow F = \frac{P_s - c}{\alpha} \quad (4)$$

where c is an arbitrary constant. We can select the value for c such that, over the input stroke of u_{\max} , no net energy is stored in the compliant component:

$$\int_{u=0}^{u=u_{\max}} f(u) du = 0 \quad (5)$$

Consequently, we take $c = P_s/2$. With v_{\max} as the prescribed output stroke, we have $\alpha = Kv_{\max}/P_s$ and the relation (4) reduces to

$$\frac{f(u)}{P_s} = \frac{1}{2} - \frac{v}{v_{\max}} \Rightarrow \frac{F}{P_s} = \frac{P_s}{2Kv_{\max}} \quad (6)$$

It is concluded that the required values of c and α for the spring mechanism depend upon the choice of actuator stall force P_s and the output stroke v_{\max} .

It is clear that the above ideal mechanisms can deliver a constant output force, but the designs are dictated by the magnitude of the actuator force P_s . Structural optimization techniques are used below to determine the structural layout of compliant mechanisms that maximize the constant output force F , at fixed input stall force P_s . The performance of the compliant mechanism for perturbed values of stall force is also explored. The behavior of these compliant mechanisms is then compared with the two idealized mechanisms above.

3 Optimization Strategy For Determining the Geometry of a Compliant Transmission Mechanism

Our task is to design a transmission mechanism that converts the actuator displacement u into a suitable output displacement v , ideally at a constant output force F . We will relax the constraints on the design of Sec. 2.2 and allow for nonlinear kinematics with energy storage in the compliant mechanism. An optimization strategy is used to search for geometric designs with the desired transmission characteristic.

3.1 Description of the Optimization Problem. Fig. 3(a) shows an actuator of stiffness K with two prescribed values of stall forces P_1 and P_2 . The topology optimization procedure generates a compliant transmission mechanism subject to a number of geometric constraints that will be explained later. The optimization procedure maximizes the output forces F_1 and F_2 with the stall force held fixed at P_1 and P_2 , respectively, as shown in Fig.

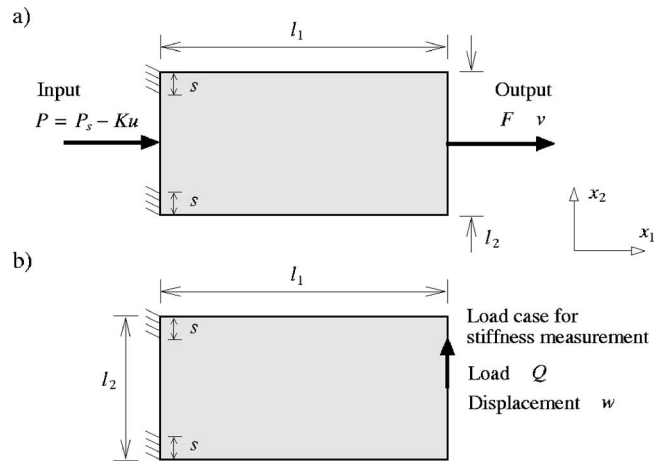


Fig. 4 The design domain for the compliant transmission mechanism. The mechanism is fully clamped on foundations of length s . (a) The actuator is modeled by the force P . At the output point the prescribed displacement v is applied in the x_1 -direction leading to the reaction force F . The mechanism is to be designed to make F constant for a prescribed maximum output displacement, v_{\max} . (b) A small transverse force Q is applied as an independently loadcase in the x_2 -direction leading to the transverse stiffness $k = Q/w$ where w is the displacement. The transverse stiffness is an imposed constraint on the compliant mechanism.

3(b). The calculations reveal that the output force is constant only at discrete values of output displacement v_i within an overall stroke v_{\max} . These discrete values of output displacement are the collocation points in the topology optimization procedure. In the example shown in Fig. 3, two such collocation points v_1 and v_2 are marked.

3.1.1 Assumed Material Properties and Constraints on Structural Realization. For the examples in this paper, we assume that the compliant mechanisms have been constructed from an isotropic elastic solid of Young's modulus E and Poisson ratio 0.25, with plane strain conditions enforced. The transmission mechanism operates with an output displacement ranging from 0 to v_{\max} . A size limitation is enforced: the rectilinear dimensions of the mechanism should not exceed l_1 by l_2 , with an out-of-plane thickness of t , and a maximum overall domain volume thereby given by $V^* = l_1 l_2 t$. Additionally, the maximum allowable volume fraction of solid material within the domain is taken to be $V/V^* = 0.3$. Numerical experimentation revealed that a high volume fraction leads to islands of material being unattached to the remainder of the mechanism. Alternatively, if an extremely low value is chosen the mechanism has insufficient stiffness to fulfill the optimization task.

Fixed displacements are prescribed over segments of length s of the mechanism, as shown in Fig. 4. An additional practical constraint on the design is a minimum value of the transverse passive stiffness k^* at the output location of the transmission mechanism. In order to calculate this stiffness, a transverse load Q is applied to the output point in a separate calculation, as sketched in Fig. 4(b). Acceptable optimized designs possess a transverse stiffness k that must exceed a minimum value k^* . As explained by Kawamoto, Bendsoe, and Sigmund [26] the constraint on k indirectly controls the number of degrees of freedom of the mechanism. An increased stiffness in the transverse direction leads to a mechanism with reduced degrees of freedom.

Dimensional analysis dictates that the nondimensional output force F/P_s depends upon the independent groups v_{\max}/l_1 , l_2/l_1 , Kl_1/P_s , Et_1/P_s and k^*l_1/P_s . In the examples given below the boundary conditions (s/l_1), geometrical properties (l_2/l_1), and

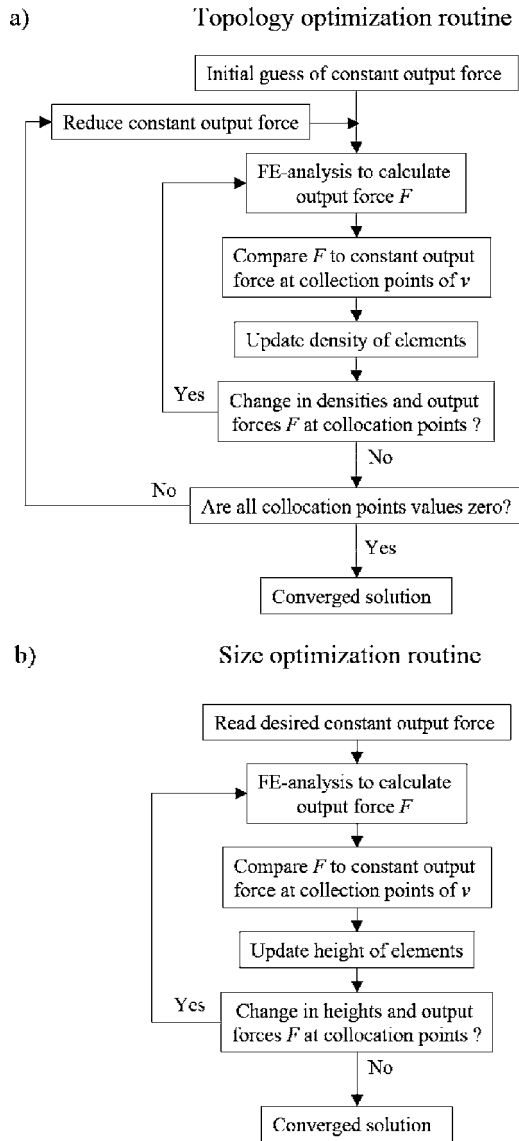


Fig. 5 Flow diagrams for (a) the topology optimization procedure and (b) the size optimization procedure.

material parameters (EtI_1/P_s) are held constant. Numerical experiments on the topology optimization reveal the sensitivity of the design to the displacement range (v_{\max}/l_1) and actuator stiffness (Kl_1/P_s).

We now explain the structural optimization techniques used to obtain compliant mechanisms having a constant output force F over a given output stroke v_{\max} .

3.2 Topology Optimization Using Continuum Modeling.

The topology of the compliant mechanism is obtained by a continuum topology optimization procedure, as shown in the flow diagram of Fig. 5(a). This procedure contains an outer iterative loop that heuristically maximizes the constant output forces and an inner iterative loop that determines the topology for a given output force (as dictated by the outer loop). The procedure is initiated by guessing high values for the required output forces F_j^* corresponding to the stall forces P_j , as shown in Fig. 3(b). The inner loop performs finite element analysis in order to calculate the actual output forces F_j as a function of the output displacements v and forces P_j . Subsequently, the inner loop changes the topology in order for the mechanism to provide uniform output

forces F_j over the stroke, with F_j equal to the required values F_j^* . The inner loop is executed until the topology and output forces F_j do not change.

The initial values of F_j^* are chosen sufficiently high that these output forces cannot be attained, and $F_j^* > F_j$. The forces F_j^* are progressively reduced in the outer loop, and the inner iterative loop is applied until a converged solution has been achieved below $F_j^* = F_j$. Additional details on the operation of each loop are now given.

3.2.1 Outer Iterative Loop. Define the error $\varepsilon_{i,j}$ between the actual force $F_j(P_j, v_i)$ of the transmission mechanism (as determined within the inner loop) and the constant output forces F_j^* (as required by the outer loop) at the collocation points v_i by

$$\varepsilon_{i,j} = \frac{F_j(P_j, v_i) - F_j^*}{F_j^*} \quad (7)$$

Here, the index i specifies the collocation point over the stroke with the total number of collocation points given by I . In the example shown in Fig. 3(b) two such collocation points are shown. The index j specifies the number of loadcases of the stall force P_j . A converged solution has been achieved when $\varepsilon_{i,j} = 0$.

Initially, in the optimization procedure the forces F_j^* are chosen to be sufficiently high that no feasible solution can be found ($\varepsilon_{i,j} \neq 0$). A heuristic scheme is applied as an outer iterative loop for reducing the forces F_j^* . The scheme is based upon the converged solution in the inner iterative loop having the errors $\varepsilon_{i,j}^{\text{old}}$ for the forces $F_j^{*,\text{old}}$. The new forces $F_j^{*,\text{new}}$ for the inner iterative loop are calculated as

$$F_j^{*,\text{new}} = (1 + \varepsilon_{\text{num},j}) F_j^{*,\text{old}} \quad \text{where} \quad \varepsilon_{\text{num},j} = \frac{1}{I} \sum_{i=1}^I \varepsilon_{i,j} \quad (8)$$

The outer iterative loop is applied until the output forces F_j attain the required values F_j^* to within a tolerance of errors $\varepsilon_{i,j} = 0.01\%$. When this has been attained, the optimization procedure is considered to have converged to the final design solution. The aim of this heuristic is to obtain as high values as possible for the constant output forces.

3.2.2 Inner Iterative Loop. The inner iterative loop finds the material distribution by continuum topology optimization, with the relative density ρ of each element as a design variable. The problem is solved using the SIMP (Solid Isotropic Material with Penalization) method (described in Bendsøe and Sigmund [10] and references therein) combined with a mesh-independency filter by Sigmund and Petersson [27]. In this approach the local material stiffness E_L of each element scales with density ρ and modulus of fully dense solid E according to $E_L = \rho^3 E$. At the optimized solution we find that most elements have either $\rho = \rho_{\min} = 10^{-3}$ and can thereby be treated as a void, or $\rho = \rho_{\max} = 1$ and can be treated as a fully dense element. Occasionally, elements converge to intermediate values of density. When the density ρ lies in the interval $\rho_{\min} \leq \rho \leq 0.01$, we treat this element as a void, and plot the element in white. When ρ lies in the interval $0.01 < \rho < 0.9$, we treat this element as partially dense with an intermediate stiffness and plot the element in gray scale. When ρ lies in the interval $0.9 \leq \rho \leq \rho_{\max}$, we treat this element as fully dense and plot it in black.

The aim of the inner iterative loop is to iterate upon the material distribution until the output forces F_j attain the desired values F_j^* , as dictated by the outer loop. This is done by minimizing the error $\varepsilon_{i,j}$ defined in (7), where the forces F_j^* are fixed for the inner loop iterations. For that purpose, the min-max formulation followed by Pedersen [16] is applied. The maximum error between F_j and F_j^* among all the load cases ($j=1, \dots, J$) of the stall force and at all collocation points ($i=1, \dots, I$) is minimized to achieve $\varepsilon_{i,j} = 0$. The topology optimization problem can be formulated as

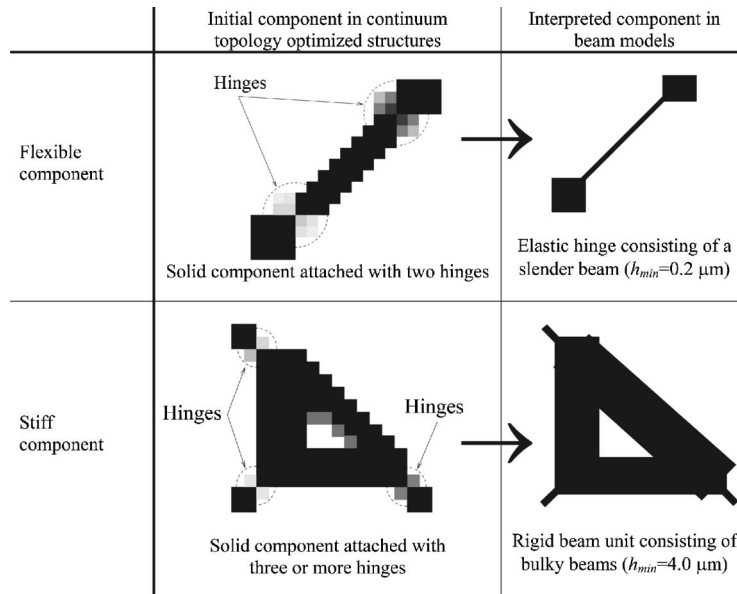


Fig. 6 Identification procedure for converting the components in the topology optimized structures into components consisting of beam elements. The beam model is used for further size optimization.

$$\begin{aligned}
 & \min: \max_{\{\rho\}}(\{\varepsilon_{i,j}\}) \text{ for } i = 1, \dots, I, \quad j = 1, \dots, J \\
 & \text{subject to } : k \geq k^*, \\
 & \quad : V \leq V^*, \\
 & \quad : \{0\} < \{\rho\}_{\min} \leq \{\rho\} \leq \{\rho\}_{\max}, \\
 & \quad : \{R\} = \{0\}
 \end{aligned} \quad (9)$$

where the vector $\{\rho\}$ contains the design variables. The vectors $\{\rho\}_{\min}$ and $\{\rho\}_{\max}$ contain the minimum and maximum values for the densities, respectively. The transverse stiffness k is constrained by k^* , as shown in Fig. 4(b). Furthermore, the material volume V is constraint by V^* . The residual for the static equilibrium of the geometrically nonlinear continuum element model, $\{R\}=\{0\}$, is determined using a combined incremental scheme and a Newton-Raphson method. The sensitivity information is determined by the adjoint method and the optimization problem is solved using the method of moving asymptotes (MMA) given in Svanberg [28]. For details about the numerical implementation, see Buhl, Pedersen, and Sigmund [29], Pedersen, Buhl and Sigmund [13], and Bruns and Tortorelli [12].

In topology optimized mechanisms, hinges often occur that resemble torsional springs or nearly frictionless joints, as illustrated in Fig. 6 (Yin and Ananthasuresh [23], Poulsen [22]; Rahmatalla and Swan [24]; also see the discussion in Bendsøe and Sigmund [10]). These hinges are often made up of two solid finite elements connected by one node and two other elements having densities close to or equal to the minimum density ρ_{\min} . The hinge resembles a pin joint with a finite rotational spring. The hinges are not desirable as they are difficult to manufacture in MEMS devices and suffer from high localized stresses. In order to avoid hinges in the present compliant mechanisms, the method suggested by Poulsen [22] was attempted. Unfortunately, the method failed to converge in the optimization algorithm. A possible reason for this is that the extra constraint for avoiding hinges is highly nonlinear, which makes the complex multiload case objective function in Eq. (9) even more complex. Thus, the presented topology optimized results contain hinges. In order to avoid these hinges in the final solutions, we adopt a second-stage size-optimization with beam elements, as described in the following section.

3.3 Size Optimization Using Beam Modeling. The topology optimized mechanisms obtained by the above method are converted into beam models, and size optimization is then conducted on the height h of each beam element. In the two-dimensional FE calculations, the mechanisms are modeled by 2-D beam elements employing a corotational Euler beam formulation; see Pedersen [17,18] for details. Typically, each beam is discretized by four elements to capture elastic buckling modes if they should occur. Mesh sensitivity studies revealed that further mesh refinements do not improve the accuracy of the calculations significantly.

The parent topology optimized mechanisms are converted into beam models using the identification procedure given in Fig. 6. Hinged units in the topology optimized mechanisms are interpreted either as slender beams or as stiff triangulated units by examining animations showing how the mechanisms deform over one stroke.

Case (i). Slender beam idealization. A topology optimized local mechanism comprises a line of solid finite elements ($\rho=1$), connected by a single node (i.e. a hinge) at each end. (Buckling of the optimized continuum models was never observed during deformation.) In the subsequent size optimization, the line of solid elements is replaced by a slender elastic beam as shown in Fig. 6. The slender beams are attached to stiff triangulated units described as follows.

Case (ii). Stiff triangulated unit. In the topology optimized structure, a solid component is identified as a group of connected elements having a relative density $\rho=1$, connected to the remainder of the structure by single nodes (i.e., a hinge) at more than two locations. This unit is converted to a stiff triangulated unit with flexible beams for attaching to the remainder of the structure in the subsequent size optimization. Again, see Fig. 6.

The beam models give a different output force characteristic than the topology optimized mechanisms. Consequently, the beam models are size optimized with the in-plane height of each beam element h as the design variable. The flow diagram for the size optimization is shown in Fig. 5(b). This flow diagram is similar to the flow diagram of the topology optimization in Fig. 5(a), except that there is no outer iterative loop maximizing the output forces. This is because the constant output forces achieved when designing the parent topology are used as the desired constant output forces F_j^* in the size optimization. Manufacturing constraints are,

however, imposed within the size optimization scheme: a minimum thickness is imposed on the heights of the beam elements. With micromachining in mind, the slender beams in Fig. 6 are restricted to have a minimum height of $0.2 \mu\text{m}$ and the stiff beams in the almost rigid beam units in Fig. 6 are restricted to have another minimum height $h_{\min}=4 \mu\text{m}$. Furthermore, the maximum allowable height for all elements is set to $h_{\max}=10 \mu\text{m}$.

The maximum error (7) between the actual output force F_j and the desired constant output force F_j^* among all the load cases ($j=1, \dots, J$) of the stall force and at all collocation points ($i=1, \dots, I$) is minimized to achieve $\varepsilon_{i,j}=0$, as shown in the flow diagram of Fig. 5(b). Then the following size optimization problem using the heights as design variables can be formulated as

$$\begin{aligned} \min: \max_{\{h\}}(|\varepsilon_{i,j}|) \text{ for } i=1, \dots, I, \quad j=1, \dots, J \\ \text{subject to } :k \geq k^*, \\ : \{h\}_{\min} \leq \{h\} \leq \{h\}_{\max}, \\ : \{R\} = \{0\} \end{aligned} \quad (10)$$

where the vector $\{h\}_{\min}$ and $\{h\}_{\max}$ contain the minimum and maximum value of the heights, respectively. Manufacturing constraints are imposed through the constraints $\{h\}_{\min}$ and $\{h\}_{\max}$. The terms k and $\{R\}$ are defined as in (9). The optimization problem of (10) is solved using the modeling and sensitivity analysis as described in Pedersen [17,18].

4 Numerical Examples for Topology Optimization

A set of topology optimizations has been performed, using representative values of actuator stiffness K , output stroke v_{\max} , geometrical properties l_2 and t , and material parameter (E) for current MEMS devices. The design domain is sketched in Fig. 4. The domain is supported over the length $s=10.0 \mu\text{m}$ at the top left corner and the bottom left corner. The size of the design domain is $l_1=200 \mu\text{m}$ by $l_2=100 \mu\text{m}$ and the thickness is $10.0 \mu\text{m}$. The mechanism is to be made from a single crystal or poly silicon of Young's modulus 160 GPa and Poisson ratio 0.25. In the present example the volume constraint is taken as $V/V^*=0.3$. The volume constraint is always active for the present examples. The stall force P_j and the actuator spring of stiffness K are applied at the center of the left edge. The prescribed displacement v and the output force F_j are both applied at the center of the right edge.

The design domain is discretized using four-noded finite elements with bilinear shape functions. Unless otherwise stated, each element has a size of $2 \mu\text{m}$ by $2 \mu\text{m}$, leading to a total of 5000 elements. The prescribed output stroke is $v_{\max}=2.0 \mu\text{m}$ or $10.0 \mu\text{m}$. The transverse stiffness requirement k^* for the mechanisms is set to be 200 N/m in line with the practical designs reviewed by Bell et al. [2].

In Sec. 4.1 we report on a mechanism optimized for several stall forces of the actuator. In Sec. 4.2 we explore the effect of actuator stiffness upon the design, and it contains a mesh sensitivity analysis. In Sec. 4.3 the maximum prescribed output displacement range v_{\max} is increased for the transmission mechanisms. And in Sec. 4.4 the sensitivity of the design to the number of collocation values of output displacement is determined.

4.1 Optimization of Output Force for Three Choices of Input Stall Force. Consider the optimization of three output forces F_j for three choices of stall force ($J=3$), with the stroke held fixed at $v_{\max}=2.0 \mu\text{m}$. All three output forces are optimized for the given set of stall forces P_j . (Note that the output force is optimized against the corresponding input force.) The result of the optimization is achieved by *mechanism A* in Fig. 7(a) using three collocation points ($I=3$). However, it can be seen from the response in Fig. 7(a) that the output force oscillates by up to 4% between the collocation points. An increase in the number of col-

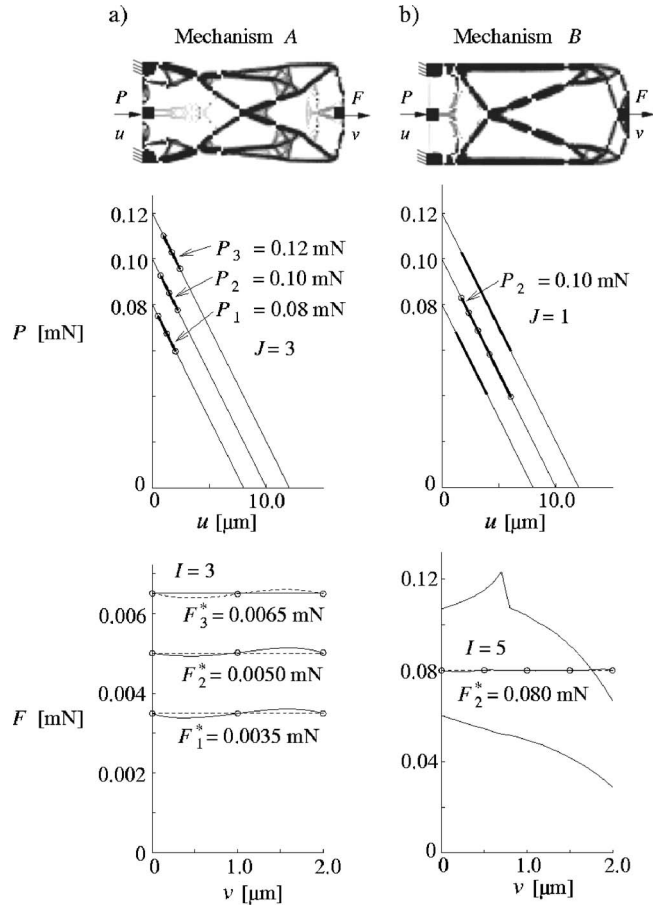


Fig. 7 (a) Mechanism A is designed to have three constant output forces using three stall forces ($J=3$). (b) Mechanism B is designed to have one constant force using one stall force ($J=1$). The circles on the output responses indicate the collocation points where the forces are measured. The circles on the input responses indicate the input response for the corresponding collocation point. ($v_{\max}=2.0 \mu\text{m}$, $K=10 \text{ N/m}$).

location points gives negligible improvement in performance. It is concluded that it is not feasible to attain a set of constant output forces corresponding to a set of stall forces. A similar conclusion has already been drawn in Sec. 2 for the pin-jointed mechanism and for the spring mechanism with linear kinematics. Convergence of the optimization algorithm is also slow when optimizing for several constant output forces, indicating that it is difficult to determine a feasible design. In the present example, over 10 000 optimization iterations were conducted, leading to over 90 000 finite element analyses. For these reasons the following examples assume a single value of stall force ($J=1$).

4.2 Optimization for a Single Stall Force. Now optimize the mechanism for a single output force using five correlation points ($I=5$), with the stall force fixed at the intermediate value $P_2=0.10 \text{ mN}$ of mechanism A in Sec. 4.1. The other parameters are identical to those already given for mechanism A. The resulting *mechanism B* is shown in Fig. 7(b). It is striking that the topology of mechanism B is significantly different from that of mechanism A. The output force of mechanism B is more than an order of magnitude higher than for mechanism A at the same level of stall force $P_s=0.10 \text{ mN}$, and the output force is much more uniform than that of mechanism A at $P_2=0.10 \text{ mN}$. However, *mechanism B* is sensitive to variations in stall force: when the optimized topology is driven by stall forces of $P_1=0.08 \text{ mN}$ and $P_3=0.12 \text{ mN}$ the output force is far from constant, see Fig. 7(b).

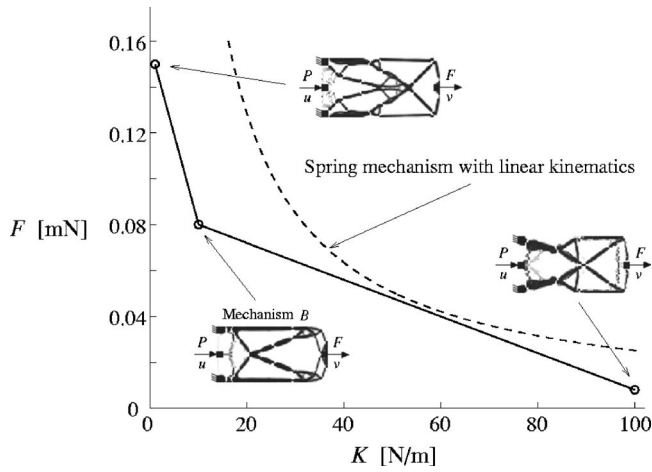


Fig. 8 Effect of actuator stiffness K upon the optimized output force. The mechanisms are designed using different values of the actuator stiffness K . ($J=1$, $P_2=0.10$ mN, $l=5$, $v_{\max}=2.0$ μm).

A mesh sensitivity study has been conducted to check if the solution of the topology optimization for mechanism B has converged with respect to the mesh discretization. Upon increasing the number of elements from 5000 to 20 000 the overall topology of mechanism B did not change and it is concluded that 5000 elements suffice.

4.3 Effect of Actuator Stiffness Upon Achieved Output Force. The sensitivity of the constant output force F to changes in the actuator stiffness K is explored, with the stall force and output stroke fixed at $P_2=0.10$ mN and $v_{\max}=2.0$ mm, respectively. Three mechanism designs for varying K are shown in Fig. 8. With increasing actuator stiffness K , the output force decreases. The output characteristic of the spring mechanism with linear kinematics (Sec. 2.2) is included in Fig. 8. It is seen that the linear mechanism outperforms the realized designs and also shows a drop in F with increasing K . However, the spring mechanism is an idealization, and has been introduced without imposing the constraints of the topology optimization. Further, it is dependent upon an initial state of prestress, which is difficult to achieve in practice.

4.4 Sensitivity of Design to Output Stroke. The sensitivity of the compliant mechanism to the output stroke is explored by designing to the same parameters as mechanism B in Fig. 7(b), but by increasing the output displacement by a factor of 5 to $v_{\max}=10$ μm . The resulting design is termed *mechanism C* and is shown in Fig. 9(a). The increase in stroke leads to a drop in output force by a factor of 10. It is also noted that the use of 5 collocation points is now insufficient to give a constant output force, compare Figs. 9(a) and 7(a). Accordingly, the number of collocation points at $v_{\max}=10$ μm is increased to 9 and this leads to *mechanism D* in Fig. 9(b); it has a more uniform output force, but at the cost of a drop in magnitude by a factor of about 4.

4.5 Transmission Ratio and Energy Efficiency of Topology Optimized Mechanisms. It is of interest to determine whether the optimized topologies possess linear or nonlinear kinematics and whether they are behaving as rigid-body, pin-jointed mechanics with no internal energy storage or as compliant mechanisms with a significant storage of energy. To address this, we consider mechanism B , which is representative of the mechanisms with a low stroke (2 μm), and mechanism C , which has a high stroke (10 μm). The kinematic ratio between the actuator displacement u and the output displacement v of the transmission mechanisms B and C are plotted in Figs. 10(a) and 10(b), respectively. It is

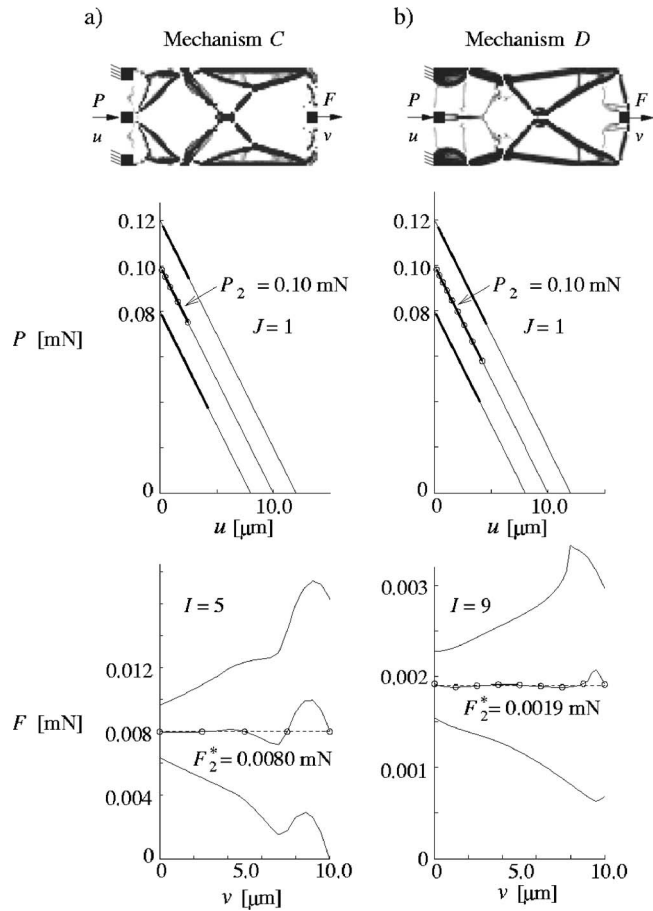


Fig. 9 The effect of the output stroke and the number of collocation points upon the optimized design. Mechanisms C and D are designed for $v_{\max}=10$ μm . Mechanism C is designed using five collocation points ($I=5$) whereas mechanism D is designed using nine collocation points ($I=9$). The circles on the output responses indicate the collocation points where the forces are measured. The circles on the input responses indicate what the input response is for the corresponding collocation points. ($J=1$, $P_2=0.10$ mN, $K=10$ N/m, $v_{\max}=10.0$ μm).

evident that both mechanisms are kinematically nonlinear.

The efficiency of each mechanism is defined by the ratio of output work to input work,

$$\eta(v) \equiv \frac{\int_0^v F(v') dv'}{\int_0^u P(u') du'}$$

Thus, $\eta=0$ denotes a transmission mechanism that delivers no work and simply stores energy. The other limit $\eta=1$ denotes a mechanism that stores no energy, such as the frictionless pin-jointed mechanism. The efficiency of the mechanisms B and C are plotted in Fig. 10. It is clear that neither mechanism is energy efficient: η rises from zero to approximately 0.4 with increasing output displacement v . The initial value of $\eta=0$ corresponds to the case of a blocked output displacement, $v=0$: in this state, the mechanisms have a finite input displacement u due to the imposed actuator force, yet the output displacement is blocked. This initial value of input displacement is evident in the plot of u vs v in Fig. 10.

The kinematics and efficiency of the rigid-body, pin-jointed mechanism outlined in Sec. 2 are included in Fig. 10, for com-

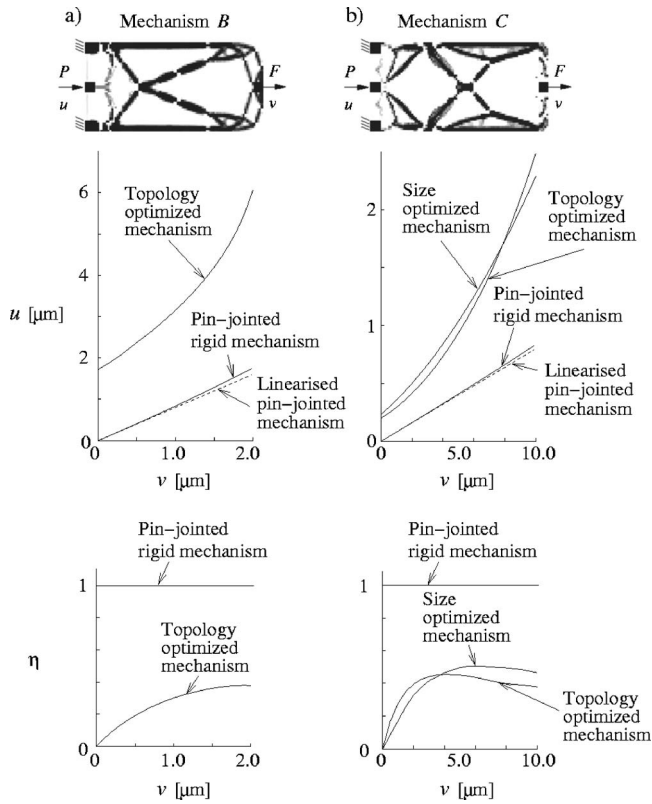


Fig. 10 The input displacement u and the energy efficiency $\eta = \int_0^v F dv' / \int_0^u P du'$ as a function of output displacement v . The mechanisms **B** and **C** are compared with the rigid-body mechanism. Mechanism **C** is also compared to a size optimized beam model solution.

parison. The pin-jointed mechanism stores no energy, giving $\eta = 1$. For both values of stroke the pin-jointed mechanism is almost linear in its kinematics. Linearized versions of the pin-jointed mechanism can be conceived, with the same initial transmission ratio (slope of u vs v curve) as that of the nonlinear pin-jointed mechanism. However, the slope of the linearized pin-jointed mechanism is about 9% less than that of the nonlinear mechanism at full stroke for the case $v_{\max} = 2 \mu\text{m}$, and 4% less than that of the nonlinear mechanism full stroke for the case $v_{\max} = 10 \mu\text{m}$. The output force F at full stroke of the linearized pin-jointed mechanisms has deviated from the desired constant values by the same percentages. It is emphasized that it is difficult to fabricate good pin-jointed rigid-body mechanisms such as the pin-jointed lever arm by micromachining.

5 Numerical Examples of Size Optimization Using Beam Modeling

The topology optimized mechanisms described above have been transformed into beam element models. The first step is to convert the continuum topology optimized mechanisms into beams models, as described in Sec. 3.3. When the topology optimized solution has a compliant hinge as sketched in Fig. 6, the set of flexible elements is replaced by a slender beam. This replacement beam behaves like a compliant hinge and is plotted in gray on the initial beam models. The initial height of this compliant beam is set to $0.4 \mu\text{m}$. When the topology optimized solution has a stiff component as shown in Fig. 6, this set of elements is replaced by bulky beams. The initial heights of these bulky beams are set to $4.0 \mu\text{m}$.

The optimization procedure of Fig. 5(b) is used to adjust the height of each beam element in order for the output force F versus

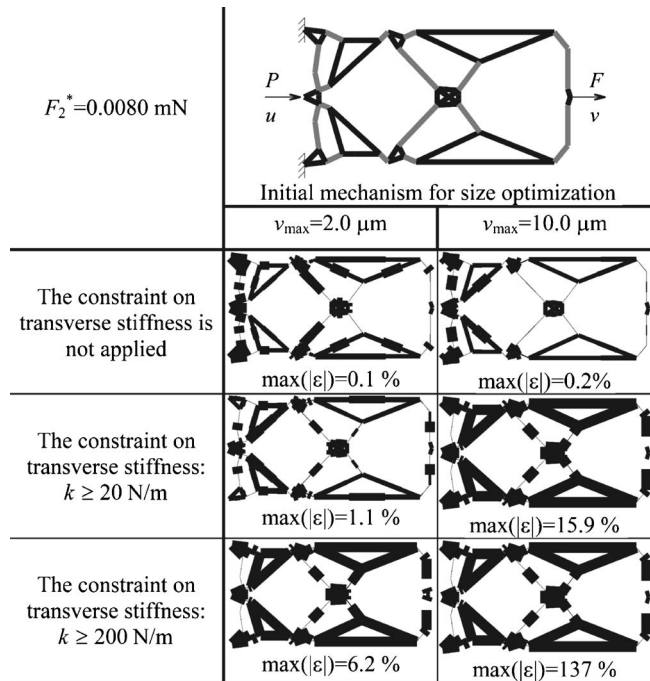


Fig. 11 Effect of maximum output displacement v_{\max} and the required transverse stiffness k upon the size optimization for a mechanism with parent topology **C**. The black elements of the initial mechanism are interpreted to be most rigid units ($h_{\min} = 4.0 \mu\text{m}$) and the gray elements are interpreted to be the most flexible parts ($h_{\min} = 0.2 \mu\text{m}$). ($J = 1$, $P_2 = 0.10 \text{ mN}$, $K = 10 \text{ N/m}$, $F_2 = 0.0080 \text{ mN}$, $l = 5$, $h_{\min} = 0.2 \mu\text{m}$).

displacement v characteristic to align as closely as possible with a constant value of output force. Here, the beam model is adjusted until the output force attains a desired constant force at collocation points. Unless otherwise stated, the desired value of output force is set to the value of output force of the parent topology optimized mechanism. Some additional optimizations are performed with the desired output force set to alternative values.

Manufacturing constraints during the size optimization are imposed through the minimum height h_{\min} and maximum h_{\max} height of the beam elements. The slender beam elements imitating hinges have a minimum height h_{\min} of $0.2 \mu\text{m}$. The beam elements in the rigid beam units have a minimum height h_{\min} of $4.0 \mu\text{m}$. The reason for the difference in minimum heights is to ensure that the characteristic of these structural units is sustained during size optimization. These minimum heights represent practical manufacturing constraints in MEMS design, with the minimum height of $h_{\min} = 0.2 \mu\text{m}$ considered as a very low minimum size in MEMS manufacture. Numerical experiments reveal that no feasible designs with constant output force could be achieved when imposing a greater minimum height upon the slender beam elements.

We limit our discussion to the transformation of the representative mechanisms **C** and **D**, as shown in Fig. 9. Recall that the stall force and stiffness of the actuator in these examples are $P_2 = 0.1 \text{ mN}$ and $K = 10 \text{ N/m}$, respectively. In Sec. 5.1, the effect of having a constraint on the transverse stiffness is examined for the parent topology of mechanism **C** of Fig. 9. The effect of a change in the desired level of output force upon the performance of a beam model derived from mechanism **C** is explored in Sec. 5.2. The importance of identifying the best beam model from the topology optimized result is addressed in Sec. 5.3 for the parent mechanism **D** of Fig. 9.

The general guidelines used to extract the beam models from the optimized continuum topologies are: (i) retain all the well

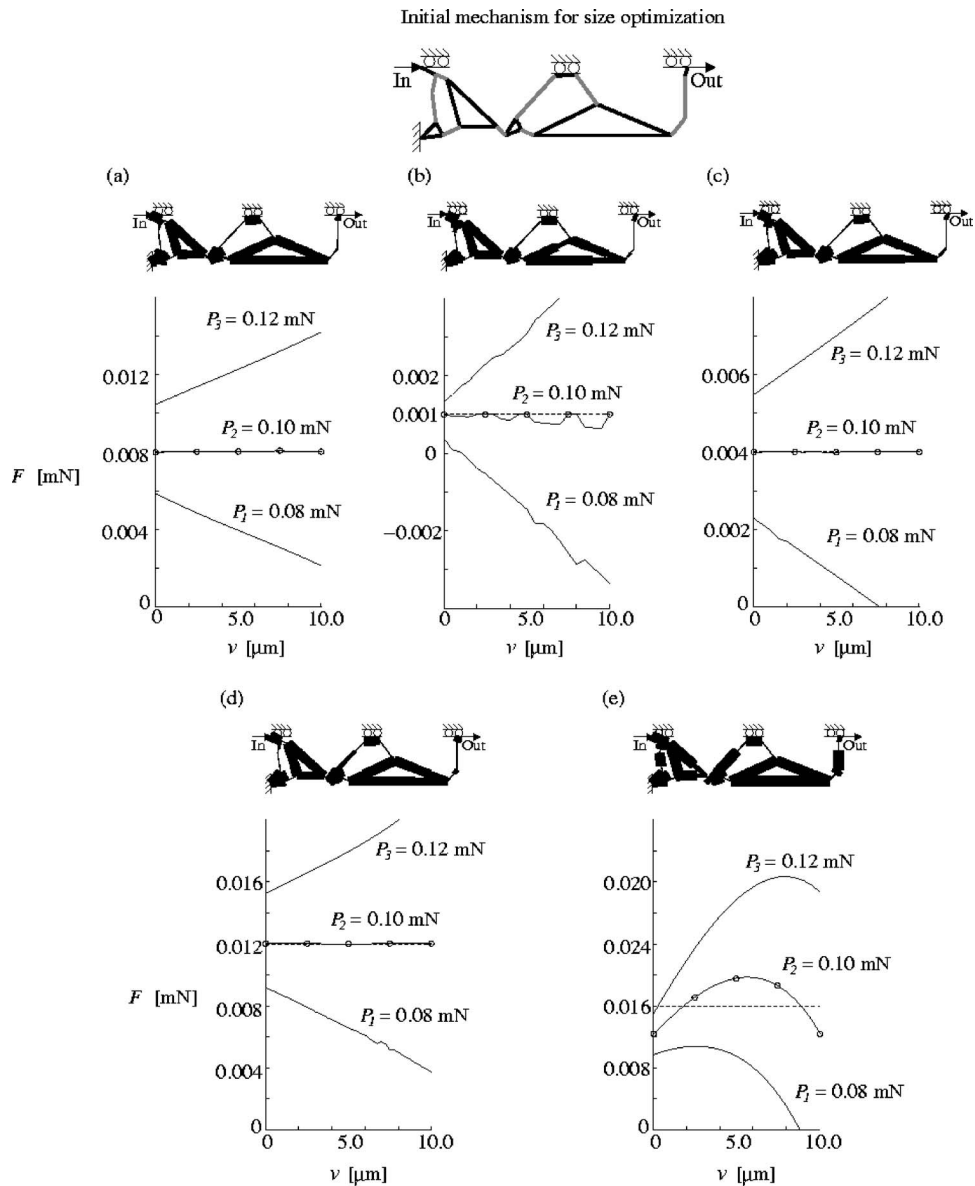


Fig. 12 Conversion of the parent topology optimized mechanism *C* in Fig. 9 into a beam model. Symmetry is applied. The black elements of the initial mechanism are interpreted to be the most rigid parts ($h_{\min}=4.0 \mu\text{m}$) and the gray elements are interpreted to be the most flexible parts ($h_{\min}=0.2 \mu\text{m}$). The mechanisms are shape optimized using the prescribed constant forces (a) $F_2^*=0.0080 \text{ mN}$, (b) $F_2^*=0.0010 \text{ mN}$, (c) $F_2^*=0.0040 \text{ mN}$, (d) $F_2^*=0.0120 \text{ mN}$, and (e) $F_2^*=0.0160 \text{ mN}$. ($J=1$, $P_2=0.10 \text{ mN}$, $K=10 \text{ N/m}$, $l=5$, $v_{\max}=10.0 \mu\text{m}$).

defined (i.e., black) regions in the exact shape, location, and orientation, (ii) retain the gray regions (except those that excluded below) that change the topology with minor deviations in shape and orientation, and (iii) ignore the gray regions if they appear inside a relatively rigid frame. Minor deviations in shape are permitted in guideline (ii) because gray regions, after size optimization, lead to flexible segments whose influence is not affected by small changes in their shape. In guideline (iii), the gray regions inside a rigid substructure has little influence on the mechanism.

5.1 Sensitivity of Beam Model Performance to the Transverse Stiffness. The beam models contain compliant hinges in the form of several slender beams. These slender beams attempt to mimic the local hinges, as sketched in Fig. 11 in the topology optimization solution. Although these slender beams have low rotational stiffness they have the deficiency that they also possess a low axial stiffness when deflected from the straight configuration,

and they possess a low buckling strength. We shall show in this section that these slender beams degrade the performance of the beam model at high values of required transverse stiffness k^* .

Consider the beam model derived from mechanism *C* of Fig. 9. The topology optimized mechanism *C* was designed for a stall force of 0.10 mN , with $k^*=200 \text{ N/m}$ and an output stroke $v_{\max}=10 \mu\text{m}$. At solution, the mechanism *C* could provide an almost constant output force of $F^*=0.008 \text{ mN}$. A size optimized beam model has been derived in order to attempt to provide the same level of output force F at 5 collocation values of output displacement. No converged solution is attained, and the optimized beam design still has a large error in output force at all the collocation points. The largest error equals 137%, and the geometry is sketched in Fig. 11. An examination of the operation of this beam mode reveals the large required value of transverse stiffness causes the beams to possess a large axial stiffness and a large

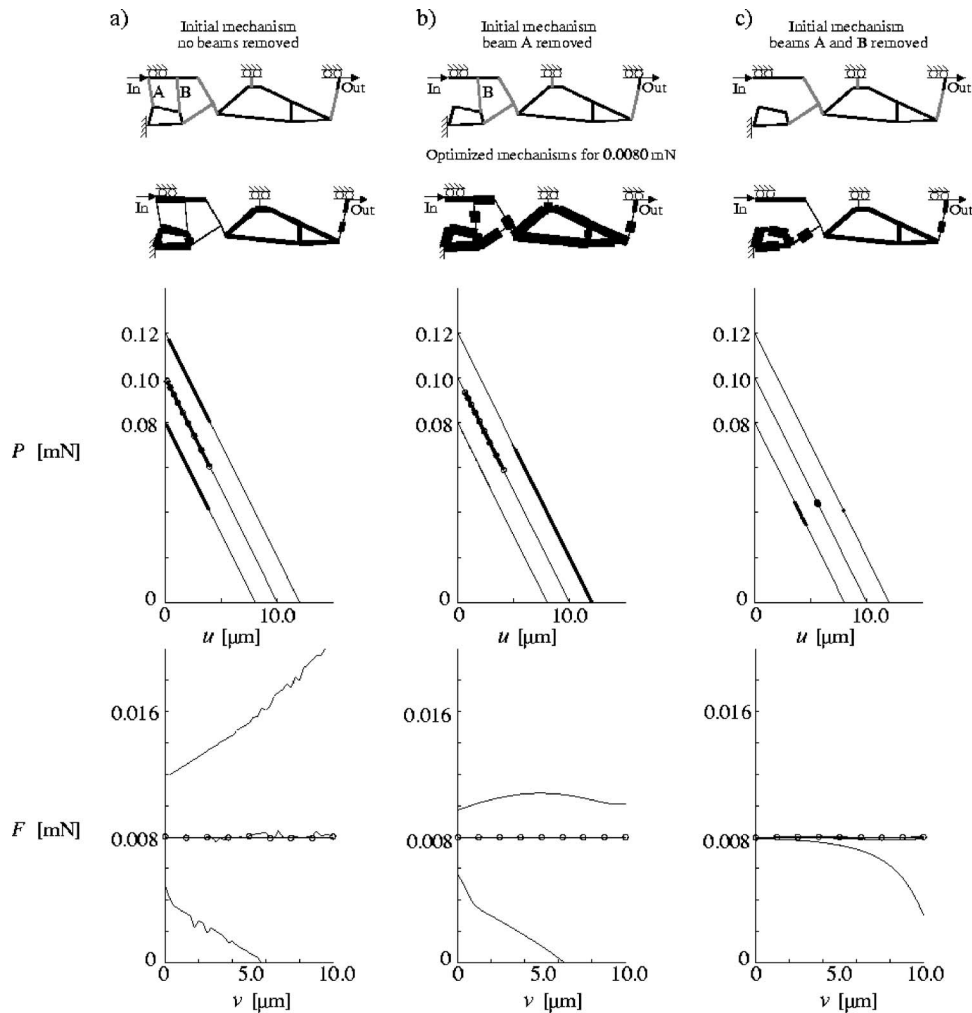


Fig. 13 Interpretation of parent topology optimized mechanism *D* in Fig. 9 into three alternative different beam models where symmetry is applied. The black elements of the initial mechanism are interpreted to be most rigid parts ($h_{\min}=4.0 \mu\text{m}$) and the gray elements are interpreted to be the most flexible parts ($h_{\min}=0.2 \mu\text{m}$). ($J=1$, $P_2=0.10 \text{ mN}$, $K=10 \text{ N/m}$, $F_2^*=0.0080 \text{ mN}$, $l=5$, $v_{\max}=10.0 \mu\text{m}$).

bending stiffness. Consequently, the beam model is not able to provide a constant output force. A reduction in the required value of k^* or a reduction in stroke v_{\max} leads to improved beam designs, with a smaller deviation in output force at the collocation points. This is summarized in Fig. 11.

Subsequently, we relax the requirement of a minimum transverse stiffness k^* in the beam models. However, we continue to use the topology optimized designs associated with $k^*=200 \text{ N/m}$ as the parent structures for the beam models.

5.2 Ability of a Beam Model to Deliver Desired Values of Constant Output Force. A size optimized beam model is shown in Fig. 12(a) derived from the topology optimized mechanism *C*. The beam model has been optimized for the same stall force of 0.10 mN, output force of $F^*=0.008 \text{ mN}$, and output stroke $v_{\max}=10 \mu\text{m}$ as that of the parent mechanism *C*. The output force of the beam model is able to achieve the desired value over the full stroke, as can be seen in Fig. 12(a). For completeness, the F vs v characteristic is shown for a variation in stall force by $\pm 20\%$. It is seen that F is no longer constant.

The height of the beams are now adjusted by size optimization at fixed topology and fixed stall force in order to obtain other constant values of output force F^* . Satisfactory designs that achieved values of F that are almost independent of v are ob-

tained, provided the desired constant force F^* is in the range 0.002 to 0.014 mN. At F^* less than 0.002 N, local elastic buckling of beam columns occurs, and the output force deviates from the desired value between the collocation points. An example is shown in Fig. 12(b), with $F^*=0.001 \text{ mN}$. In contrast, at F^* above 0.014 mN the optimization scheme cannot find a feasible design having a constant force at the collocation points, as seen in Fig. 12(e).

It is instructive to include the transmission ratio and energy efficiency of the size optimized design for the choice $F^*=0.008 \text{ mN}$ in Fig. 10(b). The behavior is very similar to that of the topology optimized design for mechanism *C*. This is a useful check on the fidelity of the beam representation.

5.3 Sensitivity of Size Optimization to the Initial Topology.

There is a degree of interpretation in the conversion from the topology optimized design to the beam model. This raises the following question: how sensitive is the behavior of the size optimized beam model to the conversion scheme adopted?

Three possible beam-model interpretations of mechanism *D* in Fig. 9(b) are shown in Fig. 13. The beam model of Fig. 13(a) is modified by removal of a beam "A" to produce the model of Fig. 13(b), and removal of two beams "A" and "B" to produce the model of Fig. 13(c). The size optimization is conducted on the

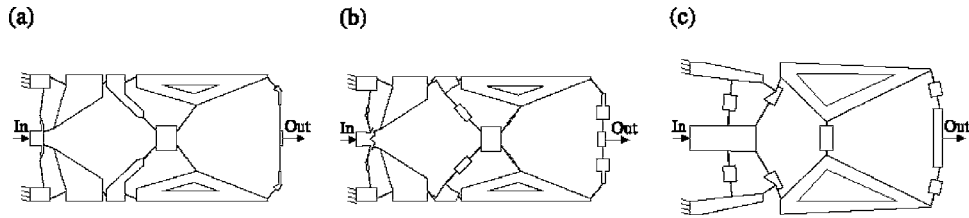


Fig. 14 (a) Continuum model of the mechanism in Fig. 12(a) ($F_2^* = 0.0120$ mN and $v_{\max} = 10.0$ μm). (b) Continuum model of the mechanism in Fig. 11 ($F_2^* = 0.0080$ mN, $v_{\max} = 2.0$ μm and $k = 20$ N/m). (c) Continuum model of the mechanism in Fig. 13(b) ($F_2^* = 0.0080$ mN and $v_{\max} = 10.0$ μm).

three beam models of Fig. 13, all for a desired output force of $F^* = 0.008$ mN. All three models can produce the desired constant force at the collocation points. However, the two optimized mechanisms in Figs. 13(a) and 13(c) are not desirable. The mechanism in Fig. 13(a) does not provide a constant output force between the prescribed displacement points. Studying the deformation of the mechanism in Fig. 13(a) shows that the two beams A and B buckle during the deformation and give rise to the oscillating load response between the displacement collocation points. However, when the two beams are eliminated in the topology, as shown in Fig. 13(c), the size-optimized mechanism behaves as a snap-through mechanism. The mechanism in Fig. 13(c) has a large initial value for the input displacement u of the actuator and energy is stored in the mechanism. The stored energy is then released and the input displacement u remains almost constant when the output displacement v is increased. Consequently, this mechanism is not desirable. Therefore, only the mechanism in Fig. 13(b) fulfills our design objective. The results in Fig. 13 show that the results of the size optimization are sensitive to small changes in the interpretation of the topology obtained by topology optimization.

5.4 Verification of Size Optimized Transmission Mechanisms. The accuracy of the beam models has been confirmed by the construction of continuum finite elements from the beam models. The finite element analysis was done using ABAQUS (Hibbitt, Karlsson, and Sorensen [25]) using eight-node biquadratic elements in plane stress with geometrical nonlinearities included. At least 20 000 elements were used in each ABAQUS representation. Figures 14(a)–14(c) give the continuum models of the mechanisms reported in Sec. 5.2 ($F_2^* = 0.0120$ mN, $P_2 = 0.10$ mN, $v_{\max} = 10.0$ μm) in Sec. 5.1 ($F_2^* = 0.0080$ mN, $P_2 = 0.10$ mN, $v_{\max} = 2.0$ μm , and $k^* = 20$ N/m) and in Sec. 5.3 ($F_2^* = 0.0080$ mN, $P_2 = 0.10$ mN, $v_{\max} = 10.0$ μm). In each case, the continuum model produced an output force that is a few percent less than that of the beam models. This discrepancy is partly due to the slightly different geometries in the two models and partly due to the differences in the beam element and continuum element modeling giving a slightly more compliant response.

6 Concluding Remarks

An optimization procedure has been introduced for designing compliant mechanisms. The mechanism serves as the transmission system for an actuator on the MEMS length scale, and is able to cancel the effects of the finite stiffness of the actuator. Thus, the mechanism converts the actuator characteristic from that of a linear drop in force under increasing displacement to one of constant output force. The examples presented are aimed at achieving a maximum value of constant output force over a given output stroke for an actuator with a prescribed stall force and stiffness. The data used for the examples focused on the electrostatic comb-drive microactuator. The designs have been achieved in two steps: topology optimization using continuum elements and size optimization using beam elements. The size optimization step was used

to remove hinge-like artifacts from the topology solution. The size-optimized solutions were validated by finite element simulations. It is demonstrated that a constant output force is achievable over a limited range of motion.

Acknowledgment

Support from the Cambridge-MIT Institute (CMI) is gratefully acknowledged. The third author (GKA) acknowledges the support of the National Science Foundation grant (No. DMI0200362).

References

- [1] Huber, J. E., Fleck, N. A., and Ashby, M., 1997, "The Selection of Mechanical Actuators Based on Performance Indices," *Proc. R. Soc. London, Ser. A*, **453**, pp. 2185–2205.
- [2] Bell, D., Lu, T., Fleck, N., and Spearing, S., 2005, "The Selection of Mems Actuators and Sensors," *J. Micromech. Microeng.*, **15**, pp. 153–164.
- [3] Nathan, R. H., 1985, "A Constant-Force Generation Mechanism," *ASME J. Mech., Transm., Autom. Des.*, **107**, pp. 508–512.
- [4] Jenuwine, J. G., and Midha, A., 1994, "Synthesis of Single-Input and Multiple-Output Post Mechanisms with Springs for Specified Energy Absorption," *J. Mech. Des.*, **116**(3), pp. 937–943.
- [5] Howell, L. L., Midha, A., and Murphy, M. D., 1994, Dimensional Synthesis of Compliant Constant-Force Slider Mechanisms, *Machine Elements and Machine Dynamics, DE-Vol. 71*, 23rd ASME Biennial Mechanisms Conference, pp. 509, 515.
- [6] Boyle, C., Howell, L. L., Magleby, S. P., and Evans, M. S., 2003, "Dynamic Modeling of Compliant Constant-Force Compression Mechanisms," *Mech. Mach. Theory*, **38**(12), pp. 1467–1487.
- [7] Ananthasuresh, G. K., Kota, S., and Gianchandani, Y., 1994, "A Methodical Approach to the Design of Compliant Micromechanisms," *Solid-State Sensor and Actuator Workshop*, pp. 189, 192. Nahar, D., and Sugar, T. G., 2003, "Compliant Constant-Force Mechanism With a Variable Output for Micro/Macro Applications," *IEEE International Conference on Robotics and Automation*, pp. 318–323.
- [8] Sigmund, O., 1997, "On The Design of Compliant Mechanisms Using Topology Optimization," *Mech. Struct. Mach.*, **25**, pp. 495–526.
- [9] Frecker, M., Ananthasuresh, G. K., Nishiwaki, S., Kikuchi, N., and Kota, S., 1997, "Topological Synthesis of Compliant Mechanisms Using Multi-Criteria Optimization," *J. Mech. Des.*, **119**(2), pp. 238–245.
- [10] Bendsoe, M. P., and Sigmund, O., 2003, *Topology Optimization—Theory, Method and Applications*, Springer-Verlag, Berlin.
- [11] Ananthasuresh, G. K., 2003, *Optimal Synthesis Methods for MEMS*, Kluwer Academic, Boston.
- [12] Bruns, T., and Tortorelli, D. A., 2001, "Topology Optimization of Nonlinear Elastic Structures and Compliant Mechanisms," *Comput. Methods Appl. Mech. Eng.*, **190**(26–27), pp. 3443–3458.
- [13] Pedersen, C. B. W., Buhl, T., and Sigmund, O., 2001, "Topology Synthesis of Large-Displacement Compliant Mechanisms," *Int. J. Numer. Methods Eng.*, **50**, pp. 2683–2706.
- [14] Saxena, A., and Ananthasuresh, G. K., 2001, "Topology Synthesis of Compliant Mechanisms for Nonlinear Force-Deflection and Curved Path Specifications," *J. Mech. Des.*, **123**, pp. 33–42.
- [15] Saxena, A., 2005, "Synthesis of Compliant Mechanisms for Path Generation Using Genetic Algorithm," *J. Mech. Des.*, **127**, p. 745.
- [16] Pedersen, C. B. W., 2003a, "Topology Optimization Design of Crushed 2D-Frames for Desired Energy Absorption History," *Struct. Multidiscip. Optim.*, **25**(5–6), pp. 368–382.
- [17] Pedersen, C. B. W., 2003b, Topology Optimization for Crashworthiness of Frame Structures, *International Journal of Crashworthiness*, **8**(1), pp. 29–39.
- [18] Pedersen, C. B. W., 2003c, "Topology Optimization of 2D-Frame Structures With Path Dependent Response," *Int. J. Numer. Methods Eng.*, **57**(10), pp. 1471–1501.
- [19] Zhou, H., and Ting, K.-L., 2005, "Topological Synthesis of Compliant

- Mechanisms Using Spanning Tree Theory,” *J. Mech. Des.*, **127**, p. 753.
- [20] Wang, M. Y., Chen, S., Wang, X., and Mei, Y., 2005, “Design of Multimaterial Compliant Mechanisms Using Level-Set Methods,” *J. Mech. Des.*, **127**, p. 941.
- [21] Howell, L., 2001, *Compliant Mechanisms*, Wiley, New York.
- [22] Poulsen, T. A., 2002, “A Simple Scheme to Prevent Checkerboard Patterns and One-Node Connected Hinges in Topology Optimization,” *Struct. Multidiscip. Optim.*, **24**, pp. 396–399.
- [23] Yin, L., and Ananthasuresh, G. K., 2003, “Design of Distributed Compliant Mechanisms,” *Mech. Based Des. Struct. Mach.*, **31**, pp. 151–179.
- [24] Rahmatalla, S., and Swan, C. C., 2005, “Sparse Monolithic Compliant Mechanisms Using Continuum Structural Topology Optimization,” *Int. J. Numer. Methods Eng.*, **62**, pp. 1579–1605.
- [25] Hibbitt, H. D., Karlsson, B. I., and Sorensen, P., 2001, *ABAQUS/Standard User’s Manual*, Version 6.2, Providence, RI.
- [26] Kawamoto, A., Bendsøe, M. P., and Sigmund, O., 2004, “Articulated Mechanism Design With a Degree of Freedom Constraint,” *Int. J. Numer. Methods Eng.*, **61**(9), pp. 1520–1545.
- [27] Sigmund, O., and Petersson, J., 1998, “Numerical Instabilities in Topology Optimization: A Survey on Procedures Dealing With Checkerboards, Mesh-Dependencies and Local Minima,” *Struct. Optim.*, **16**, pp. 68–75.
- [28] Svanberg, K., 1987, “The Method of Moving Asymptotes—A New Method for Structural Optimization,” *Int. J. Numer. Methods Eng.*, **24**, pp. 359–373.
- [29] Buhl, T., Pedersen, C. B. W., and Sigmund, O., 2000, “Stiffness Design of Geometrically Non-Linear Structures Using Topology Optimization,” *Struct. Multidiscip. Optim.*, **19**(2), pp. 93–104.